

Newton-Krylov continuation of amplitude-modulated rotating waves in sheared annular electroconvection

Gregory M. Lewis* and Jamil Jabbour

*Faculty of Science, University of Ontario Institute of Technology,
2000 Simcoe Street North, Oshawa, Ontario, Canada, L1G 0C5*

M.C. Pugh

*Department of Mathematics, University of Toronto,
40 St. George St., Toronto, Ontario, Canada, M5S 2E4*

Stephen W. Morris

*Department of Physics, University of Toronto,
60 St. George St., Toronto, Ontario, Canada, M5S 1A7*

(Dated: November 12, 2021)

Abstract

We investigate the flow transitions that occur in sheared annular electroconvection using Newton-Krylov numerical bifurcation techniques based on time-integration. In particular, we study a model that simulates the flow of a liquid crystal film in the smectic A phase suspended between two annular electrodes, and subjected to an electric potential difference and a radial shear. Due to the layered structure of the smectic A phase, the fluid can be treated as two-dimensional and is modeled using the 2-D incompressible Navier-Stokes equations coupled with an equation for charge continuity. Newton-Krylov methods are implemented for the parameter continuation of steady axisymmetric flow, rotating waves and amplitude-modulated rotating waves, with the electric Rayleigh number as the parameter. In particular, we present a defining system for the computation of the amplitude-modulated rotating waves that does not require a linearized code, and that exploits the rotational nature of the flow. The linear stability of the solutions is computed to identify the value of the electric Rayleigh number at which the transition from axisymmetric flow to rotating waves and the subsequent transition to amplitude-modulated rotating waves occur. Finally, we locate the tertiary transition and show that it corresponds to a period-4 bifurcation of the amplitude-modulated rotating waves.

I. INTRODUCTION

Much can be learned about the fundamental properties of natural fluid systems, such as the atmosphere, by studying laboratory experiments that isolate certain key aspects of the system and ignore others that do not determine the essential character of the flow. One such classical example is the differentially heated rotating fluid annulus experiment [1–5], in which a fluid is placed in a rotating cylindrical annulus while the inner and outer walls of the annulus are held at different temperatures. The fluid flow undergoes successive transitions upon variation of the temperature difference and/or the rotation rate; transitions are observed from axisymmetric flow to rotating waves, then to amplitude-modulated rotating waves (often called amplitude vacillating flow) or other forms of modulated rotating waves, and eventually to irregular flows. The flows observed in the laboratory experiments resemble those observed in the atmosphere [3].

* Contact for G.M. Lewis: Greg.Lewis@ontariotechu.ca

Another example of an experiment that has geophysical relevance is sheared annular electroconvection, in which a thin liquid crystal film suspended between two annular electrodes is driven to convection by an applied potential difference while a shear is imparted through a rotation of the inner electrode. In this system, radial electrical forces play the role of radial gravity-driven thermal buoyancy in a geophysical context. The system is a close analogue of some laboratory-scale geophysical flow experiments, e.g. those mentioned above [1, 2] (see also [6]), and to simplified models of the rotating equatorial regions of planetary atmospheres and planetary interiors [7, 8]. Although sheared annular electroconvection shares many characteristics with these counterparts, including their $SO(2)$ symmetry, a crucial difference is in the two-dimensional nature of electroconvection. In particular, the electroconvection experiments employ a liquid crystal in smectic A phase, which can essentially be considered to be a two-dimensional fluid. In addition to providing insight into transition phenomena in buoyancy driven rotating flows, this is an ideal system in which to study bifurcations in spatiotemporal pattern formation [9].

Laboratory and numerical studies of sheared annular electroconvection [10–17] have observed that under small electric potential difference, the system exhibits axisymmetric flow in which the velocity of the fluid is in the azimuthal direction and the electric current is carried only by conduction between the annular electrodes, while the surface charge remains undisturbed by the flow. At a critical potential difference, a primary transition occurs to rotating waves in which the charge is also convected by the flow, increasing the total current beyond that of pure conduction. Beyond this critical potential difference, it is observed that the system undergoes successive transitions similar to those observed in the differentially heated annulus, in particular, transitions from the rotating wave state to modulated rotating waves [14], to localized vortices [15], and subsequently to unsteady turbulent flow [16, 17], are observed.

Here, we use numerical bifurcation methods to compute the primary, secondary and tertiary transitions in a mathematical model of sheared annular electroconvection. In particular, we use numerical continuation to follow the solutions corresponding to the steady axisymmetric flow, rotating waves, and amplitude-modulated rotating waves, and determine transitions from a linear stability analysis of these solutions. In relation to numerical experimentation, i.e. using time-stepping simulations alone, such bifurcation techniques are able to compute unstable solutions, and are able to unambiguously and accurately determine the

range of parameters over which a flow is stable, even when the ranges are small. Bifurcation methods can also determine regions of bistability without relying on finding specific initial conditions that lead to the different stable solutions. Moreover, they can provide insight into the mechanism of the flow transitions themselves. They can determine the type of bifurcation associated with the transition, even in the case of subcritical bifurcations. Thus, a clearer picture of the dynamics of the system can be discovered. However, the advantages of this approach are balanced by the increase in the required computational resources.

The steady axisymmetric flow corresponds to a steady solution of the model equations, while the rotating waves and amplitude-modulated rotating waves correspond to periodic orbits and invariant tori, respectively. Numerical methods have been developed for the parameter continuation of such solutions in large-dimensional systems, with special interest in applications to fluid dynamics; see, e.g. [18] for a review. Some such methods, e.g., [19–21], are based on time-integration of the dynamical system. These methods can be useful, in particular, when a time-stepping (i.e. simulation) code is already available, as is often the case. The method of Tuckerman and Barkley [21] effectively uses the linear part of the time-stepping code as a preconditioner to solve for steady solutions of the model equations; this method, however, cannot be generally used to compute periodic orbits. The approach of Sanchez et al. [19, 20] formulates the solution of the relevant flows as fixed points of maps, and can be used to compute steady solutions and periodic orbits, and can be extended for the computation of invariant tori.

In the current application, it is possible to use the rotational property of the flow to aid in the reduction of the computational cost. In particular, our approach uses the observation that the rotating waves are relative equilibria with respect to a rotating reference frame. Consequently, the rotating waves can be computed as steady solutions with an additional unknown, corresponding to the constant phase speed of the rotating wave. This approach has been used extensively in the context of fluid dynamics; see, e.g., [18, 22–25]. Not common is the application to amplitude-modulated rotating waves, which are periodic orbits when viewed in an appropriately defined rotating reference frame. This idea has been used by [26] to compute such solutions in thermal convection in a spherical shell. We use a similar approach here. In particular, we use a Newton-Krylov method based on time-integration, in a formulation in which the rotating waves and modulated rotating waves are computed as fixed points of a discrete dynamical system (a map) [19]. Stability of the flows can be

determined in terms of the stability of the fixed points of the map. Here, unlike [26], we do not use a linearized version of the code in the computations, but instead use a finite-difference approximation. This requires the use of an alternative auxiliary condition for the defining system used in the numerical continuation of the modulated rotating waves. The advantage of our approach is that the numerical simulation code is only required to act as a ‘black-box’, i.e. it can be used directly without modification, which significantly simplifies the implementation. In addition, unlike [26], our computations require the use of preconditioning because the natural preconditioning, which is discussed in [19], is not sufficient.

In Section II, we provide details of the electroconvection experiment and of the mathematical and numerical models used in the study. In Section IV, we introduce the methods, and discuss some details of the implementation. The results and discussion are presented in Section V.

II. ELECTROCONVECTION

Electroconvection refers to fluid flows generated by electrical forces acting on space charges within the fluid, or on surface charges at the interfaces between fluids [27]. Here, we will be concerned with convection of thin liquid films driven by surface charges. Smectic A liquid crystals are layered materials that naturally form stable suspended films composed of weakly conducting organic liquids. In the smectic A phase, the elongated molecules arrange themselves into layers with their long axes oriented perpendicular to the layers. A layer is of nano-meter thickness and, within a layer, the oriented molecules move freely as in a normal Newtonian viscous liquid, while molecular motion between layers is very restricted, as in a soft solid. A suspended smectic A film has a submicron film thicknesses and consists of an integer number of discrete molecular layers that move together as a nearly ideal 2-D fluid and strongly resist variations in the film thickness. When suspended between electrodes, the films readily form surface charges that interact with the electric field to produce flow; the film can span a distance between electrodes on the order of millimeters.

Many laboratory experiments on electroconvecting smectic A films, using various geometries, have been reported, including rectangular geometry [28–31], annular geometry [13], and annular films with an applied shear [10–12, 32]. Here, we consider the experiment of

Tsai et al. [12] which employed a smectic A film suspended between two concentric annular electrodes. The inner electrode is rotated at a constant speed ω_i , imposing a radial shear, and a DC voltage V is applied between the two electrodes. The working fluid was 8CB (4-cyano-4'octylbiphenyl) [12], which is in the smectic A phase at room temperature.

The standard experimental protocol of Tsai et al. [12] consisted of measuring the current I between the electrodes as the applied DC voltage V is incremented from zero to a maximum value in small steps, and then similarly decremented back to zero, with the inner anode rotating at a prescribed constant angular speed ω_i and the outer cathode stationary and grounded. For relatively low voltage, the fluid flow is axisymmetric. In this state, the velocity of the fluid is in the azimuthal direction where the flow lines are concentric circles and the current passes between the electrodes by conduction. However, when the applied voltage V exceeds a critical voltage V_c , the fluid becomes arranged into symmetric pairs of convective vortices. At higher voltages, more complicated flows are provoked.

It is shown in [11, 12], that the primary transition to convection is supercritical for different rotation rates, i.e. the amplitude of the observed convective vortices grows monotonically from zero. Furthermore, the rotation acts as a stabilizer of the flow, delaying the onset of convection.

These transitions have been reproduced with numerical simulations [14, 17]. The numerical experiments consisted of long-time integrations using a random perturbation from the base state solution (axisymmetric flow) as the initial condition. Simulations were conducted for a wide range of the Rayleigh number \mathcal{R} , defined below, while fixing the other nondimensional parameters. In addition to reproducing the transition from the axisymmetric flow to rotating waves, a secondary transition from rotating waves to amplitude-modulated rotating waves was found.

A. The Mathematical Model

In the physical experiment, the thin film is confined in an annular region defined in circular cylindrical coordinates (r, θ, z) as, $r_i \leq r \leq r_o$; see Figure 1. The film is a liquid crystal in smectic A phase with uniform thickness s , and gap width $d = r_o - r_i$. Since $s \ll d$, the film is treated as a 2D electrically conducting Newtonian fluid lying in the plane $z = 0$. The density, dynamic viscosity and conductivity of the fluid are denoted by ρ, η and σ

respectively. The inner electrode, $0 \leq r \leq r_i$, $z = 0$, is rotating at a constant angular speed ω_i and is held at a constant electric potential V . The outer electrode, $r \geq r_o$, $z = 0$, is held at zero potential and does not rotate. The conservation of momentum and the conservation of matter, given by the incompressible Navier-Stokes equations with an electric body force $q\mathbf{E}$, model the velocity field $\mathbf{u}(r, \theta, t) = u(r, \theta, t)\hat{\mathbf{r}} + v(r, \theta, t)\hat{\boldsymbol{\theta}}$

$$\rho \left(\frac{\partial \mathbf{u}}{\partial t} + (\mathbf{u} \cdot \nabla) \mathbf{u} \right) = -\nabla P + \eta \nabla^2 \mathbf{u} + q\mathbf{E}, \quad (1a)$$

$$\nabla \cdot \mathbf{u} = 0, \quad (1b)$$

where $\hat{\mathbf{r}}$ is the unit vector in the radial direction, $\hat{\boldsymbol{\theta}}$ is the unit vector in the azimuthal direction, ∇ is the 2D gradient operator, P is the pressure, q is the surface charge density, $\mathbf{E} = -(\nabla\psi)|_{z=0}$ is the electric field in the film plane $z = 0$, and ψ is the 3D electric potential which extends both above and below the film. The conservation of charge is expressed by the continuity equation

$$\frac{\partial q}{\partial t} = -\nabla \cdot \mathbf{J}, \quad \mathbf{J} = \sigma\mathbf{E} + q\mathbf{u}, \quad (1c)$$

where the current density \mathbf{J} is composed of an ohmic conduction term $\sigma\mathbf{E}$, and a convective term $q\mathbf{u}$ due to the fluid motion. The 3D electric potential ψ satisfies the Laplace equation

$$\left(\nabla^2 + \frac{\partial^2}{\partial z^2} \right) \psi = 0, \quad (1d)$$

in the charge-free region $z \neq 0$. To find the charge in the film region $z = 0$, we note that the 2D surface charge density q satisfies Maxwell's equation [30]

$$q = -2\epsilon_0 \frac{\partial \psi}{\partial z} \Big|_{z=0^+}, \quad (1e)$$

where ϵ_0 is the permittivity of free space. The currents are sufficiently small that magnetic effects may be neglected. The factor of two in (1e) arises from accounting for the charge accumulation on the both sides of the film.

Equations (1a)–(1e) are subject to the following boundary conditions. At each electrode, the velocity field satisfies no-slip boundary conditions

$$\mathbf{u} = \omega_i r_i \hat{\boldsymbol{\theta}}, \quad r = r_i, \quad (2a)$$

$$\mathbf{u} = 0, \quad r = r_o. \quad (2b)$$

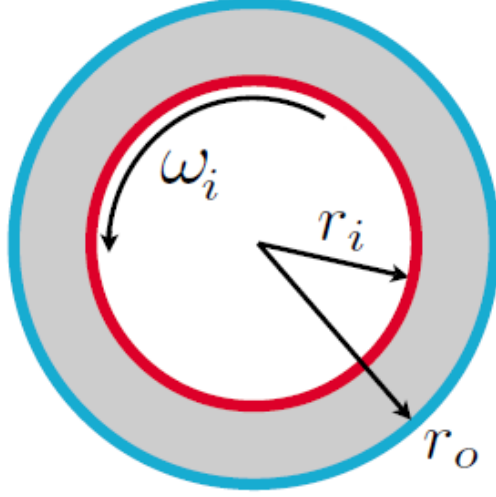


FIG. 1. The geometry of sheared annular electroconvection. The liquid crystal is confined in an annular region $r_i \leq r \leq r_o$, and the inner electrode rotates at a constant rate ω_i .

The potential ψ is set to zero at infinity

$$\lim_{z \rightarrow \pm\infty} \psi(r, \theta, z) = 0, \quad (2c)$$

and, at $z = 0$, takes on the imposed voltage, so that

$$\psi(r, \theta, 0) = \psi_2(r, \theta) = \begin{cases} V, & \text{for } r \leq r_i, \\ 0, & \text{for } r \geq r_o, \end{cases} \quad (2d)$$

where ψ_2 is the 2D electric potential in the $z = 0$ plane.

A stream function/vorticity formulation can be used to eliminate the pressure term in (1a). We define the stream function $\phi = \phi(r, \theta, t)$ and vorticity $\omega = \omega(r, \theta, t)$ as follows

$$\mathbf{u} = \nabla \phi \times \hat{\mathbf{z}}, \quad \nabla \times \mathbf{u} = \omega \hat{\mathbf{z}}, \quad (3)$$

and use these to replace the velocity vector \mathbf{u} as dependent variables. In addition, we can define a characteristic length, time and charge. If we let the imposed voltage V denote a representative voltage over a length scale of $d = r_o - r_i$ and a relaxation time $\tau_c = \epsilon_0 d / \sigma$, where σ is the conductivity and ϵ_0 is the permeability of free space, then we obtain the following nondimensionalization

$$r = d\tilde{r}, \quad \phi = \frac{\sigma d}{\epsilon_0} \tilde{\phi}, \quad \psi = V\tilde{\psi}, \quad t = \tau_c \tilde{t}, \quad q = \frac{\epsilon_0 V}{d} \tilde{q}, \quad (4)$$

where the tilde represents the dimensionless variables. Applying the formulation (3) to (1a)–(1e), nondimensionalizing with (4), and dropping the tilde, we obtain the system of equations describing the evolution of the dimensionless physical quantities, i.e. the vorticity ω , stream function ϕ , charge density q , the 2D potential in the fluid ψ_2 and the 3D potential ψ :

$$\nabla^2 \phi = -\omega, \quad (5a)$$

$$\frac{\partial \omega}{\partial t} + (\mathbf{u} \cdot \nabla) \omega = \mathcal{P} \nabla^2 \omega + \mathcal{P} \mathcal{R} (\nabla \psi_2 \times \nabla q) \cdot \hat{\mathbf{z}}, \quad (5b)$$

$$\frac{\partial q}{\partial t} + (\mathbf{u} \cdot \nabla) q = \nabla^2 \psi_2, \quad (5c)$$

$$\left(\nabla^2 + \frac{\partial^2}{\partial z^2} \right) \psi = 0, \quad q = -2 \frac{\partial \psi}{\partial z} \Big|_{z=0^+}, \quad (5d)$$

where the nondimensional parameter groups are the Rayleigh number \mathcal{R} and Prandtl number \mathcal{P} defined as

$$\mathcal{R} = \frac{\epsilon_0^2 V^2}{\sigma \eta}, \quad \mathcal{P} = \frac{\epsilon_0 \eta}{\rho \sigma d}, \quad (6)$$

respectively. The Rayleigh number \mathcal{R} , which is proportional to the square of the applied voltage V , describes the relative strength of the applied electric forcing to the viscous dissipation, and the Prandtl number \mathcal{P} is a fluid parameter that describes the ratio of the charge relaxation time to the viscous relaxation time.

The dimensionless boundary conditions become

$$\frac{\partial}{\partial r} \phi(r_o, \theta) = 0, \quad \phi(r_o, \theta) = 0, \quad (7a)$$

$$\frac{\partial}{\partial r} \phi(r_i, \theta) = -\frac{\omega r_i \epsilon_0}{\sigma} = -\omega_i r_i \tau_c, \quad \phi(r_i, \theta, t) = g(t), \quad (7b)$$

$$\psi_2(r_i, \theta) = 1, \quad \psi_2(r_o, \theta) = 0, \quad (7c)$$

$$\psi(r, \theta, 0) = \begin{cases} 1, & \text{for } 0 \leq r \leq r_i, \\ \psi_2(r, \theta), & \text{for } r_i \leq r \leq r_o, \\ 0, & \text{for } r \geq r_o, \end{cases} \quad (7d)$$

$$\lim_{z \rightarrow \pm \infty} \psi(r, \theta, z) = 0, \quad (7e)$$

where r_i, r_o are dimensionless quantities scaled by d and the tilde have once again been dropped for clarity. The radial component of the no-slip boundary condition implies that the stream function is independent of θ at the boundaries; it is determined up to a (possibly

time-dependent) constant. If there were only one boundary, one could set the stream function to be zero at that boundary. As there are two boundaries, we are still able to choose the stream function at the outer boundary to be zero, but, then, we need to determine the stream function at the inner boundary (i.e. the function $g(t)$) from the flow; see (7b). The width of the film in dimensionless units is then $r_o - r_i = 1$, where r_o is the dimensionless radius of the outer electrode set at zero electric potential and r_i is the dimensionless radius of the inner electrode set at an electric potential of 1. It is convenient to express the radii of the annular geometry with the aspect ratio $\alpha = r_i/r_o$. Introducing this, the dimensionless radii can be expressed as

$$r_i = \frac{\alpha}{1 - \alpha}, \quad r_o = \frac{1}{1 - \alpha}. \quad (8)$$

It remains to determine $g(t)$ in (7b). It is related to the total azimuthal flux as follows:

$$\int_{r_i}^{r_o} v(r, \theta, t) dr = \phi(r_i, \theta, t) - \phi(r_o, \theta, t) = g(t) \implies g(t) = \int_{r_i}^{r_o} \widehat{v}_0(r, t) dr. \quad (9)$$

Above, \widehat{v}_0 denotes the zeroth Fourier coefficient of the Fourier series of v ; the Fourier coefficients are functions of r and t . It satisfies the following partial differential equation

$$\frac{\partial \widehat{v}_0}{\partial t} + \left(u \frac{\partial v}{\partial r} \right)_0 + \frac{1}{r} (\widehat{uv})_0 = \mathcal{P} \left(\frac{1}{r} \frac{\partial \widehat{v}_0}{\partial r} + \frac{\partial^2 \widehat{v}_0}{\partial r^2} - \frac{1}{r^2} \widehat{v}_0 \right) - \frac{\mathcal{P} \mathcal{R}}{r} \left(q \frac{\partial \widehat{\psi}_2}{\partial \theta} \right)_0, \quad (10)$$

which is found by computing the angular average of the angular component of (1a). Integrating (10) with respect to r yields an ODE for $g(t)$, closing the system

$$\frac{dg}{dt} = \int_{r_i}^{r_o} \mathcal{P} \left(\frac{1}{r} \frac{\partial \widehat{v}_0}{\partial r} + \frac{\partial^2 \widehat{v}_0}{\partial r^2} - \frac{1}{r^2} \widehat{v}_0 \right) - \frac{\mathcal{P} \mathcal{R}}{r} \left(q \frac{\partial \widehat{\psi}_2}{\partial \theta} \right)_0 - \left(u \frac{\partial v}{\partial r} \right)_0 - \frac{1}{r} (\widehat{uv})_0 dr. \quad (11)$$

Equations (5a)–(5d) with the boundary conditions (7a)–(7e), (11) describe the sheared annular electroconvection of any arrangement of 2D thin conductive film freely suspended in empty space. In other words, the model still holds for the unsheared electroconvection with appropriate changes to the boundary conditions.

1. The deviation equations

The rotation of the inner electrode generates an axisymmetric steady Couette shear, which is observed at low \mathcal{R} . The flow is characterized by a dimensionless Reynolds number

$$\text{Re} = \frac{r_i \Omega}{\mathcal{P}}, \quad (12)$$

where $\Omega = \tau_c \omega_i$ is the dimensionless angular frequency of the inner electrode. We call this flow the base state and denote it by a superscript zero. This flow can be computed analytically by considering only steady axisymmetric solutions of (5a)–(5d) with boundary conditions (7a)–(7e). In particular, the base state is given by

$$\frac{\partial \phi^{(0)}(r)}{\partial r} = \text{Re} \mathcal{P} \frac{\alpha}{1 + \alpha} \left(r - \frac{r_o^2}{r} \right), \quad (13a)$$

$$\omega^0(r) = 0, \quad (13b)$$

$$q^{(0)}(r) = \frac{2}{\ln \alpha} \left(\frac{1}{r_o} F \left(\frac{1}{2}, \frac{1}{2}; 1; \frac{r^2}{r_o^2} \right) - \frac{1}{r} F \left(\frac{1}{2}, \frac{1}{2}; 1; \frac{r_i^2}{r_o^2} \right) \right), \quad (13c)$$

$$\psi_2^{(0)}(r) = \begin{cases} 1, & \text{for } 0 \leq r \leq r_i, \\ \frac{\ln(r/r_o)}{\ln(r_i/r_o)}, & \text{for } r_i \leq r \leq r_o, \\ 0, & \text{for } r \geq r_o, \end{cases} \quad (13d)$$

$$\psi^{(0)}(r, z) = \int_0^\infty A(k) J_0(kr) e^{-kz} dk, \quad (13e)$$

where F is a hypergeometric function [10], J_0 is the zeroth Bessel function and

$$A(k) = k \int_0^\infty \psi^{(0)}(r, 0) J_0(kr) r dr. \quad (14)$$

Equation (13a) can be integrated from r_i to r_o to obtain an explicit form for $\phi^{(0)}$ that satisfies the boundary condition (7b) with

$$g(t) = g^{(0)} = \text{Re} \mathcal{P} \frac{\alpha}{\alpha^2 - 1} \left(\frac{\alpha + 1}{2} + \frac{1}{1 - \alpha} \ln(\alpha) \right). \quad (15)$$

We note that, in this experiment, the inner electrode is rotating at a constant rate while the outer electrode is fixed. However, independent rotations of the electrodes can be dealt with by applying a transformation to a rotating frame of reference, where the outer electrode is stationary. The Coriolis forces introduced by the transformation can be absorbed into the pressure term of (1a).

Using the axisymmetric base state, we can view the solutions as the sum of the base state and the deviation from the base state:

$$q(r, \theta, t) = q^{(0)}(r) + q^{(1)}(r, \theta, t), \quad (16)$$

and likewise for the other dependent variables. It is convenient to rewrite the equations in terms of the deviations, $\psi^{(1)}$ and $q^{(1)}$, instead of their counterparts, ψ and q , respectively.

Upon applying this decomposition and substituting into (5c)–(5d), we obtain equations which govern the evolution of the deviations $\psi^{(1)}$ and $q^{(1)}$.

$$\frac{\partial q^{(1)}}{\partial t} + \frac{1}{r} \left(\frac{\partial q^{(0)}}{\partial r} \frac{\partial \phi^{(1)}}{\partial \theta} + \frac{\partial q^{(1)}}{\partial r} \frac{\partial \phi^{(1)}}{\partial \theta} - \frac{\partial \phi^{(0)}}{\partial r} \frac{\partial q^{(1)}}{\partial \theta} - \frac{\partial \phi^{(1)}}{\partial r} \frac{\partial q^{(1)}}{\partial \theta} \right) - \nabla^2 \psi_2^{(1)} = 0, \quad (17a)$$

$$\left(\nabla^2 + \frac{\partial^2}{\partial z^2} \right) \psi^{(1)} = 0, \quad q^{(1)} = -2 \frac{\partial \psi^{(1)}}{\partial z} \Big|_{z=0}. \quad (17b)$$

The deviation variables, $\psi_2^{(1)}$ and $\psi^{(1)}$, satisfy the following boundary conditions

$$\psi_2^{(1)}(r_i, \theta) = \psi_2^{(1)}(r_o, \theta) = 0, \quad (18a)$$

$$\psi^{(1)}(r, \theta, 0) = \begin{cases} 0, & \text{for } 0 \leq r \leq r_i, \\ \psi_2^{(1)}(r, \theta), & \text{for } r_i \leq r \leq r_o, \\ 0, & \text{for } r \geq r_o, \end{cases} \quad (18b)$$

$$\lim_{z \rightarrow \pm\infty} \psi^{(1)}(r, \theta, z) = 0. \quad (18c)$$

Thus, equations (5a)–(5b), (11), (17a)–(17b) with boundary conditions (7a)–(7b), (18a)–(18c) form a closed set of equations describing the flow of the liquid crystal.

III. THE NUMERICAL SOLVER

In this section, we provide a brief overview of the numerical time-stepper, which is implemented in MATLAB [17], that will be used in our computations. The solutions of the evolution equations (5a)–(5b), (11), (17a)–(17b) with boundary conditions (7a)–(7b), (18a)–(18c) are approximated with a pseudospectral method. In particular, the 2D physical quantities, the stream function ϕ , the vorticity ω , the charge density deviation $q^{(1)}$ and the electric potential deviation $\psi_2^{(1)}$, are approximated using a truncated Fourier series $\{e^{im\theta}\}$ in the $\hat{\theta}$ direction and a truncated Chebyshev series $\{T_n(r)\}$ in the \hat{r} direction. That is, we write

$$\phi(r, \theta, t) = \sum_{n=0}^{N_c} \sum_{m=-K}^K \tilde{\phi}_{nm}(t) e^{im\theta} T_n(x), \quad (19)$$

and similarly for the other physical quantities, where K is the highest Fourier mode, N_c is the order of the highest Chebyshev polynomial and

$$x = 2r - \frac{1 + \alpha}{1 - \alpha}, \quad (20)$$

linearly maps $r \in [\frac{\alpha}{1-\alpha}, \frac{1}{1-\alpha}]$ to $x \in [-1, 1]$.

The AB/BDI2 time-stepping scheme

$$\frac{3\mathbf{u}^{(k+1)} - 4\mathbf{u}^{(k)} + \mathbf{u}^{(k-1)}}{2\delta t} \approx \frac{\partial \mathbf{u}}{\partial t} = \mathcal{L}(\mathbf{u}) + \mathcal{N} \approx \mathcal{L}(\mathbf{u}^{(k+1)}) + 2\mathcal{N}^{(k)} - \mathcal{N}^{(k-1)}, \quad (21)$$

is implemented, where δt is a prescribed time step and $\mathbf{u}^{(k)}$ is the spatially discretized solution vector at the k th time-step (see e.g. [33]). This scheme is a second-order implicit-explicit method, in which the nonlinear part \mathcal{N} is treated explicitly and the linear part $\mathcal{L}(u)$ is treated fully implicitly. It has also be referred to as semi-implicit BDF (SBDF) or extrapolated Gear [34, 35].

The two-step method (21) requires two initial values; the first is given, while the second must be approximated. In the context of the bifurcation methods discussed in IV, it is necessary that this second step is sufficiently accurate. To this end, a hierarchy of discretizations is used. Specifically, a one-step first-order scheme is used with a very small time-step to generate a preliminary second initial step. The two-step method is then used, with sequentially increasing step size, to generate an approximation of the solution at $t = \delta t$, which is used as the second initial step at the desired step size δt used for the rest of the calculation.

The numerical time-stepper for the smectic electroconvection is complicated by a non-standard boundary condition. The surface charge q is not only coupled to flow motion, but also regulated by the 2D electric potential field ψ_2 . To handle this situation, a different approach is required to resolve the nonlocal coupled electric body force that involves Maxwell's equation (17b) which connects the charge density with the electric potential. However, the nonlocal calculation of the 3D potential and the charge field are coupled instantaneously and therefore do not involve any time derivatives. The Laplace equation is solved implicitly in integral form where the boundary condition is resolved by decomposing the field using a pseudospectral technique [17].

With the proper initial conditions, boundary conditions and time step, the 2D electric potential ψ_2 is computed simultaneously with the surface charge q by means of the nonlocal mapping. The vorticity ω can then be obtained from the computed q and ψ_2 leading to the computation of the stream function ϕ . The Orszag 3/2 aliasing rule is performed when dealing with the nonlinear terms.

For a more detailed explanation of the time-stepper, the reader is referred to [17]. The method we use is essentially the same, except that in [17], it is the evolution equations

governing the deviations from the base state of the stream function $\phi^{(1)}$ and vorticity $\omega^{(1)}$, that are time-stepped, rather than the full ϕ and ω as in our formulation. Also in [17], the approximation that $\phi^{(1)}(r_o, t) = \phi^{(1)}(r_i, t) = 0$ is made [36]. We do not make this approximation, i.e. we do not assume that $g(t) = g^{(0)}$. We, therefore, need to discuss the time-stepping of (11), starting from (9) for the full stream function ϕ .

From (9), $g(t)$ is the radial integral of $\widehat{v}_0(r, t)$. We time-step (10) to find $\widehat{v}_0^{(k+1)}$ and then use Chebyshev-Gauss quadrature to approximate the radial integral, thus determining $g^{(k+1)}$. The time-stepping is done as follows. First, the velocity components $u^{(k-1)}$, $u^{(k)}$, $v^{(k-1)}$, and $v^{(k)}$ are determined from the stream function $\phi^{(k-1)}$ and $\phi^{(k)}$. The nonlinear terms $u \frac{\partial v}{\partial r}$, uv , and $q \frac{\partial \psi_2}{\partial \theta}$ are computed at the $(k-1)$ st and k th time levels. Applying the FFT and then selecting the component that approximates the zeroth Fourier coefficient determines the nonlinear terms of (10): $\widehat{\mathcal{N}}^{(k-1)}_0$ and $\widehat{\mathcal{N}}^{(k)}_0$. The time-stepping (21) is then applied to (10), determining $\widehat{v}_0^{(k+1)}$.

IV. METHODS

After spatial discretization using the spectral methods described above, our model can be written as a continuous dynamical system in the general form

$$\mathcal{M} \frac{d\mathbf{u}}{dt} = \mathbf{F}(\mathbf{u}, \mu), \quad \mathbf{F} : \mathbb{R}^n \times \mathbb{R} \rightarrow \mathbb{R}^n, \quad (22)$$

where $\mathbf{u} = \mathbf{u}(t) \in \mathbb{R}^n$ is the discretized solution vector, μ is a real parameter, and the matrix \mathcal{M} may not be invertible due to algebraic constraints. Here, the solution vector \mathbf{u} contains the four physical quantities (the electric potential ψ_2 , the charge density q , the vorticity ω , and the stream function ϕ), and has size $n = 4(2K + 1)(N_c + 1)$, where K is the highest Fourier mode and N_c is the highest degree of Chebyshev polynomial as shown in Section III.

A. Computation of rotating waves

The solutions of the continuous dynamical system (22) corresponding to rotating waves can be computed as fixed points of a flow map Φ_t :

$$\mathbf{u} \rightarrow \Phi_t(\mathbf{u}, \mu), \quad \Phi_t : \mathbb{R}^n \times \mathbb{R} \times \mathbb{R} \rightarrow \mathbb{R}^n, \quad (23)$$

where $\Phi_t(\mathbf{u}, \mu)$ is given by the solution of (22) at time $t \in \mathbb{R}$, given an initial condition $\mathbf{u} \in \mathbb{R}^n$ and a fixed parameter $\mu \in \mathbb{R}$. In particular, the rotating waves are limit cycles, and thus, such solutions of (22) must satisfy $\mathbf{u}(t) = \mathbf{u}(t + \tau_w)$, where τ_w is the period of the limit cycle. Therefore, the flow map $\Phi_{\tau_w}(\mathbf{u}, \mu)$ will map \mathbf{u} to itself, for any \mathbf{u} on the limit cycle, and thus the rotating waves can be found as fixed points of the map Φ_{τ_w} by solving

$$\Phi_{\tau_w}(\mathbf{u}, \mu) - \mathbf{u} = 0, \quad (24)$$

where τ_w is to be determined. This method, however, requires each integration of the map to be over a full period τ_w , and therefore, we choose, instead, a less general, but more efficient, approach. In particular, we use the property that the rotating waves are relative equilibria, i.e., integration through any time t is equivalent to rotation by $\tilde{\theta} = wt$, where w is the constant phase speed of the wave. Therefore, all points \mathbf{u} on the rotating wave must satisfy

$$\Phi_t(\mathbf{u}, \mu) - \gamma \mathbf{u} = 0, \quad (25)$$

where the rotation operator $\gamma \in SO(2)$ acts on \mathbf{u} via $\gamma \mathbf{u} = \mathbf{u}(r, \theta - wt)$, the phase speed w is to be determined, and t is arbitrary and thus may be taken to be much smaller than the period τ_w .

Equation (25) defines the rotating wave up to a phase, and therefore, to obtain uniqueness, we introduce the phase condition

$$\frac{\partial}{\partial \theta} \mathbf{u}^{(0)} \cdot (\mathbf{u} - \mathbf{u}^{(0)}) = 0, \quad (26)$$

which chooses the phase relative to a reference solution $\mathbf{u}^{(0)}$, usually chosen to be the initial guess used for the nonlinear solver (see below). The phase condition ensures that we seek corrections to $\mathbf{u}^{(0)}$ that are orthogonal to the tangent to the symmetry generator $\frac{\partial}{\partial \theta} \mathbf{u}^{(0)}$, the derivative of $\mathbf{u}^{(0)}$ with respect to θ . We choose to seek corrections orthogonal to $\mathbf{u}^{(0)}$ instead of \mathbf{u} to remove the complication of working with an extra nonlinear equation.

The nonlinear system given by (25) and (26) can then be solved using the Newton-Raphson method, in which case updates $\left[\delta \mathbf{u}_j^{(k)}, \delta w_j^{(k)} \right]$ at each iteration k are found from

the linear system

$$\begin{bmatrix} D_{\mathbf{u}}\Phi_t(\mathbf{u}_j^{(k)}, \mu_j) - \gamma \ t \frac{\partial \mathbf{u}_j^{(k)}}{\partial \theta} \\ \frac{\partial \mathbf{u}^{(0)}}{\partial \theta} & 0 \end{bmatrix} \begin{bmatrix} \delta \mathbf{u}_j^{(k)} \\ \delta w_j^{(k)} \end{bmatrix} = \begin{bmatrix} \mathbf{u}_j^{(k)} - \Phi_t(\mathbf{u}_j^{(k)}, \mu_j) \\ \frac{\partial \mathbf{u}^{(0)}}{\partial \theta} (\mathbf{u}_j^{(k)} - \mathbf{u}^{(0)}) \end{bmatrix}, \quad (27a)$$

$$\mathbf{u}_j^{(k+1)} = \mathbf{u}_j^{(k)} + \delta \mathbf{u}_j^{(k)}, \quad (27b)$$

$$w_j^{(k+1)} = w_j^{(k)} + \delta w_j^{(k)}, \quad (27c)$$

where the subscript j labels points along the solution curve Γ , and $D_{\mathbf{u}}\Phi_t$ is the Jacobian of the map Φ_t . The matrix in the linear system (27a) is of size $(n+1) \times (n+1)$, that is, it is only a single row and column larger than the matrices required for the numerical integration, but it is dense and computational intensive to compute. However, the action of the Jacobian $D_{\mathbf{u}}\Phi_t$ on a vector $\delta \mathbf{u}$ can be found from the evolution of an initial perturbation $\delta \mathbf{u}$ as determined by the model equations linearized about the solution \mathbf{u} . Thus, if GMRES [37], or some other iterative method, is used to solve the linear system (27a), it is not necessary to form the Jacobian explicitly, because such methods only require knowledge of matrix-vector products involving the Jacobian. As such, each iteration of the linear solve involves a time-integration of the linearized model equations (i.e. the solution of a variational problem).

If code for the linearization is not available, the action of $D_{\mathbf{u}}\Phi_t$ on $\delta \mathbf{u}$ can be approximated using a finite-difference method, e.g., the forward finite-difference approximation can be used

$$D_{\mathbf{u}}\Phi_t(\mathbf{u}, \mu)\delta \mathbf{u} \approx \frac{\Phi_t(\mathbf{u} + \epsilon \delta \mathbf{u}, \mu) - \Phi_t(\mathbf{u}, \mu)}{\epsilon}, \quad (28)$$

for some $\epsilon > 0$. Thus, the action of $D_{\mathbf{u}}\Phi_t$ on the vector $\delta \mathbf{u}$ can be approximated given knowledge of the action of Φ_t on the vectors $(\mathbf{u} + \epsilon \delta \mathbf{u})$ and \mathbf{u} . That is, using the approximation (28), each matrix-vector product in the linear solve can be computed from two evaluations of Φ_t . However, one of the two are the same for each GMRES iteration, and therefore, only a single time integration is required per iteration.

In general, in order to ensure convergence of the solution of the linear system in a reasonable number of iterations, preconditioning is required. We discuss this in Section IV C. The computation of the derivative with respect to the angle θ and the action of the rotation operator γ on the vector $\delta \mathbf{u}$ are computed in spectral space as an element-wise multiplication using the Fast Fourier Transform (FFT). As a result, the main cost in this computation is the time-integration, approximated using the time-stepping code.

These systems can be adapted very simply to incorporate pseudo-arclength continuation [18]. However, we choose to implement natural continuation as we do not observe any limit points along the solution branches.

B. Computation of amplitude-modulated waves

Amplitude-modulated rotating waves correspond to invariant 2-tori in phase space, and resemble rotating waves with the exception that their amplitude varies periodically in time. As such, we can use an extended version of the approach used to compute the rotating waves. In particular, we replace integration for arbitrary time t with integration for time τ the unknown period of the oscillation of the wave amplitude. That is, an amplitude-modulated rotating wave has the property that integration for time τ will be equivalent to rotation by angle $w\tau$. In this case, there are two unknown parameters, namely, the phase speed w and the unknown period τ of the amplitude, while there are also two phases that need to be specified, namely, the phase of the wave, and the phase of the amplitude oscillation. To fix the phase of the wave, we use the criterion (26) as we did for the rotating waves, while to fix the phase of the amplitude, we consider only corrections to our initial guess that are orthogonal to the initial guess (29c); essentially this selects an amplitude of the solution. Other possibilities exist for this second condition; see [26]. As such, the amplitude-modulated rotating waves can be found from the defining system:

$$\Phi_\tau(\mathbf{u}, \mu) - \gamma \mathbf{u} = 0, \quad (29a)$$

$$\frac{\partial}{\partial \theta} \mathbf{u}^{(0)} \cdot (\mathbf{u} - \mathbf{u}^{(0)}) = 0, \quad (29b)$$

$$\mathbf{u}^{(0)} \cdot (\mathbf{u} - \mathbf{u}^{(0)}) = 0, \quad (29c)$$

where τ is the (unknown) period of the amplitude oscillations, $\gamma \mathbf{u} = \mathbf{u}(r, \theta - w\tau, \tau)$, w is the phase speed. The phase speed itself does not need to be constant; in particular, we can interpret w as a mean phase speed for which $\tilde{\theta} = w\tau$ gives the angle of rotation required for (29a) to be satisfied.

This system is solved using the same approach as used for the rotating waves. In particular, the linear system to be solved for each Newton-Raphson iteration is similar to that for the rotating wave (27), and is solved with GMRES, using (28) to approximate the action of the Jacobian $D_{\mathbf{u}}\Phi$. The linear system contains only a single extra equation, i.e. the am-

plitude phase equation (29c), and the Jacobian $D_{\mathbf{u}}\Phi$ is the same size as in (27). Generally, the period τ is much longer than the arbitrarily chosen t , and therefore, the computation of the amplitude-modulated waves requires significantly more computation time, but is no more memory-intensive.

C. Preconditioning

As described above, the linear systems for the Newton-Raphson iterations can be solved with GMRES. If the spectrum of the matrix associated with the linear system is well clustered, then it may not be necessary to introduce preconditioning to reduce the number of GMRES iterations required to obtain convergence in a reasonable number of iterations. Generally for dissipative system, the spectrum is expected to become more clustered around the origin as the integration time increases because most of the eigenvalues of the Jacobian $D_{\mathbf{u}}\Phi_t$ correspond to damped perturbations, and thus, for sufficiently long integration times, preconditioning is not required [19]. However, for the current application, we find that even for relatively long integration times, the number of GMRES iterations required for convergence is prohibitively many, and thus preconditioning is required.

Because we do not have an explicit form for the matrix $D_{\mathbf{u}}\Phi_t$, we cannot use most standard preconditioners. However, we can construct $D_{\mathbf{u}}\Phi_t$ column by column, for the linearization about a particular solution \mathbf{u} and for a particular value of the parameter μ , because $[D_{\mathbf{u}}\Phi_t] \mathbf{e}_i = i\text{th column of } D_{\mathbf{u}}\Phi_t$, where \mathbf{e}_i is the i th standard basis vector. If using the approximation (28), this process requires $n + 1$ evaluations of Φ_t to compute, and is therefore not practical to construct for each Newton-Raphson iteration. We can, however, use it as a preconditioner. In particular, we find that it works well as a preconditioner for all Newton-Raphson iterations, over a large range of parameters. Thus, although expensive to compute initially, it can be used for many computations. Furthermore, an accurate approximation of $D_{\mathbf{u}}\Phi_t$ is not required, and therefore, significant efficiency is obtained by computing it using time steps that are an order of magnitude larger than for the computation of the solutions themselves. Also, although $D_{\mathbf{u}}\Phi_t$ is dense, it does not require prohibitively more memory than the matrices involved in the numerical integration itself, due to the use of spectral methods.

D. The Eigenvalue Problem

The steady solutions, which are given by $(\mathbf{u} = 0, \mu)$ when written in terms of deviations from the base state, and the rotating wave solutions (\mathbf{u}, w, μ) described above can be computed as fixed points of the flow map $\Phi_t(\mathbf{u}, \mu)$; for the steady solutions, t is arbitrary, while for the rotating waves, t is the period τ_w of the corresponding solution, which can be computed from $w\tau_w = 2\pi/m$, where m is the primary azimuthal wave number observed in the rotating wave. Thus, the stability of the solutions can be determined from the spectrum of $D_{\mathbf{u}}\Phi_t(\mathbf{u}, \mu)$, the linearization of the flow map $\Phi_t(\mathbf{u}, \mu)$ about fixed points \mathbf{u} . In particular, for maps, a fixed point is said to be *linearly stable* if all eigenvalues of the Jacobian $D_{\mathbf{u}}\Phi_t(\mathbf{u}, \mu)$ lie in the unit circle of the complex plane, and *unstable* if at least one eigenvalue lies outside the unit circle. Bifurcations of the system occur when an eigenvalue crosses the unit circle as a parameter is varied.

The amplitude-modulated rotating wave solutions $(\mathbf{u}, w, \tau, \mu)$ are fixed points of the map $\gamma^{-1}\Phi_\tau(\mathbf{u}, \mu)$, where τ is the period of the amplitude oscillations. The linear stability of these solutions can also be found from the eigenvalues of $\gamma^{-1}D_{\mathbf{u}}\Phi_\tau(\mathbf{u}, \mu)$.

We use the Implicitly Restarted Arnoldi Method (IRAM) to compute the relevant eigenvalues of $D_{\mathbf{u}}\Phi_t(\mathbf{u}, \mu)$, where the IRAM is an iterative method that computes approximations of the eigenvalues of largest magnitude of a matrix using only matrix-vector products [38, 39]. Thus, its implementation together with (28) enables us to compute the relevant eigenvalues, i.e. those of largest magnitude, without explicitly forming $D_{\mathbf{u}}\Phi_t(\mathbf{u}, \mu)$. We use the IRAM MATLAB implementation `eigs`.

V. RESULTS AND DISCUSSION

We consider the Rayleigh number \mathcal{R} as a bifurcation parameter, and apply the methods described in Section IV. The results are presented in the bifurcation diagram of Figure 2. The relevant physical and numerical parameters used for the computations are presented in Table I.

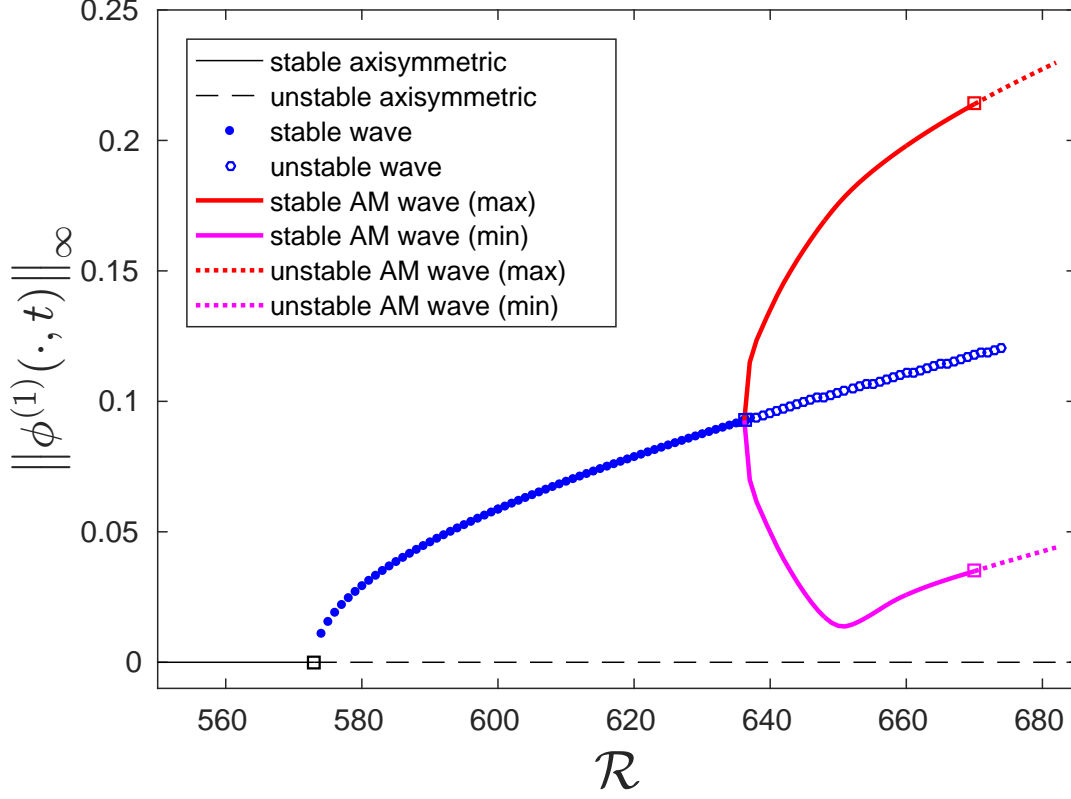


FIG. 2. The bifurcation diagram with Rayleigh number \mathcal{R} as parameter. Solutions are represented in terms of $\|\phi^{(1)}(\cdot, t)\|_\infty$, the infinity norm of the stream function deviation at a particular time (spatial maximum of $|\phi^{(1)}|$), i.e. the wave amplitude. For the amplitude-modulated (AM) rotating waves, the maximum (red) and minimum (magenta) amplitude of the solution over a period of the amplitude oscillations is plotted. The squares represent the critical parameter values, i.e. the bifurcation points. Values for other parameters are listed in Table I.

A. Axisymmetric flow and the primary transition

For all values of the Rayleigh number, the base state (axisymmetric solution) is given by (13); in terms of the deviations, this solution corresponds to the zero solution. Computation of the eigenvalues of the map $D_{\mathbf{u}=0}\Phi_t$ reveals a primary bifurcation from the base state at a critical Rayleigh number $\mathcal{R}_{c1} = 573.0$; see Figure 2. In particular, at \mathcal{R}_{c1} , a supercritical Neimark-Sacker bifurcation of the flow map Φ_t occurs, at which a complex conjugate pair of eigenvalues has modulus 1, and for $\mathcal{R} < \mathcal{R}_{c1}$, all eigenvalues have modulus less than 1 [40]. The bifurcating solutions exist for $\mathcal{R} > \mathcal{R}_{c1}$ and correspond to stable rotating waves with

TABLE I. The parameters used in the numerical results.

| Model parameters | | |
|---|---|--------------------|
| Symbol | Parameter | Value |
| \mathcal{P} | Prandlt number | 75.8 |
| Re | Reynolds number | 0.249 |
| α | Aspect ratio | 0.56 |
| Time-stepper: discretization parameters | | |
| Symbol | Parameter | Value |
| N_c | Highest order of the Chebyshev basis | 24 |
| K | Highest Fourier wave number | 32 |
| δt | Time step | 1×10^{-4} |
| δt_P | Time step for preconditioner calculation | 1×10^{-3} |
| Numerical bifurcation parameters | | |
| Symbol | Parameter | Value |
| t | Arbitrary integration time | 0.1 |
| ϵ | Perturbation amplitude of the forward finite difference approximation | 10^{-3} |
| New_tol | Newton-Raphson residual tolerance: | 10^{-8} |
| gmres_tol | GMRES tolerance | 10^{-6} |

azimuthal wave number six (see Figure 3); the wave has constant (positive) phase speed and constant amplitude, i.e. as time evolves, the solution maintains its shape and rotates counter-clockwise at a constant rate. See Supplemental Material at [URL will be inserted by publisher] for an animation of the stream function deviation $\phi^{(1)}$ corresponding to the rotating wave solution at $\mathcal{R} = 600$. We discuss the parameter continuation of the rotating waves in Section V B.

The value of t used in the computation of the eigenvalues is arbitrary; we use a value $t = 0.2$, which provides convergence in a reasonable number of iterations. Increasing the value of t increases the separation of the eigenvalues, enabling convergence in fewer iterations, but also increases the cost per iteration. We find that the linear stability analysis is not

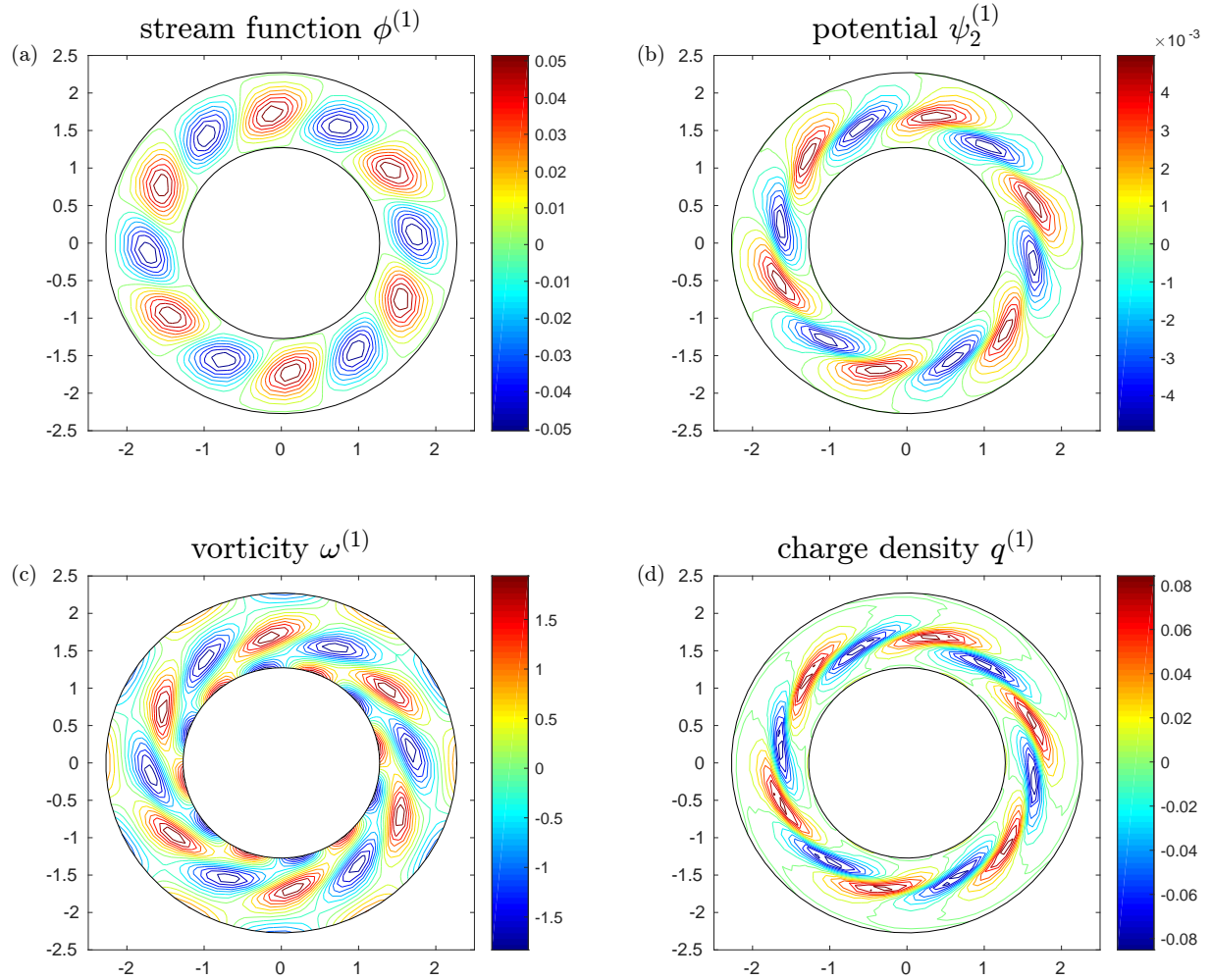


FIG. 3. Rotating wave solution at Rayleigh number $\mathcal{R} = 600$. A snapshot of the deviations from the base state of the four physical quantities are shown: (a) the stream function $\phi^{(1)}$; (b) the 2D electric potential $\psi_2^{(1)}$; (c) the vorticity $\omega^{(1)}$; and (d) the charge distribution $q^{(1)}$. The solution maintains this shape and rotates counter-clockwise at a constant phase speed (see Supplemental Material at [URL will be inserted by publisher] for an animation of the stream function deviation $\phi^{(1)}$).

sensitive to the choice of t . The linear stability is determined from the computation of the eigenvalues with the 20 largest magnitudes, and the critical value \mathcal{R}_{c1} is computed to a tolerance of 10^{-2} using a secant method. Other parameters are held fixed at the values listed in Table I.

B. Rotating waves and the secondary transition

The rotating wave solutions, observed for $\mathcal{R} > \mathcal{R}_{c1}$, satisfy (25)–(26), while their linear stability can be determined from the spectrum of $D_{\mathbf{u}}\Phi_{\tau_w}$, where $\tau_w = 2\pi/(mw)$ is the period of the rotating wave, and w and m are its phase speed and primary azimuthal wave number, respectively. As we continue the rotating wave solution in the Rayleigh number \mathcal{R} , the amplitude of the rotating wave grows from zero at $\mathcal{R} = \mathcal{R}_{c1}$ as shown in Figure 2, while the phase speed w does not vary significantly along the branch; specifically, the phase speed w decreases monotonically from 5.45 at $\mathcal{R} = \mathcal{R}_{c1}$ to 5.44 at $\mathcal{R} = 674$.

Along the branch, a secondary bifurcation is detected at a critical Rayleigh number $\mathcal{R}_{c2} = 636.2$, where again a complex conjugate pair of eigenvalues crosses the $|z| = 1$ curve in the complex plane, while for $\mathcal{R}_{c1} < \mathcal{R} < \mathcal{R}_{c2}$, all eigenvalues have modulus 1 or less [41]; see Figure 4. This bifurcation of the map Φ_{τ_w} is supercritical and of type Neimark-Sacker. In this case, the bifurcating solution corresponds to a 2-torus in the phase space, and a modulated rotating wave for the governing equations. The eigenfunction corresponding to the critical eigenvalue, shown in Figure 4, resembles a wave with azimuthal wave number 6, and thus, we expect that the bifurcating solution is amplitude modulated (also referred to as amplitude vacillating wave), which we confirm using simulations. These solutions resemble a rotating wave with wave number six (see Figure 3) whose amplitude oscillates periodically in time, except that there is a slight tilting of the vortices when the amplitude is at its lowest. See Supplemental Material at [URL will be inserted by publisher] for an animation of the stream function deviation $\phi^{(1)}$ corresponding to the amplitude-modulated rotating wave solution at $\mathcal{R} = 660$. Generally, these solutions are quasi-periodic, and trajectories in the phase space are dense on the 2-torus. That is, the amplitude-modulated wave never quite returns to its starting values, although it will get arbitrarily close. The solution at the end of a period of the amplitude oscillations is a rotated version of the solution at the beginning of the period; this is true regardless of the number of periods. However, at isolated points along the solution branch, in particular when the frequency of amplitude oscillations is rationally related to the frequency of the oscillations due to the rotating wave, the solution is periodic. In this case, there are an infinite number of periodic solutions; phase shifts of the periodic solution at any point in time correspond to other periodic solutions. We discuss the parameter continuation of the amplitude-modulated rotating waves in Section V C.

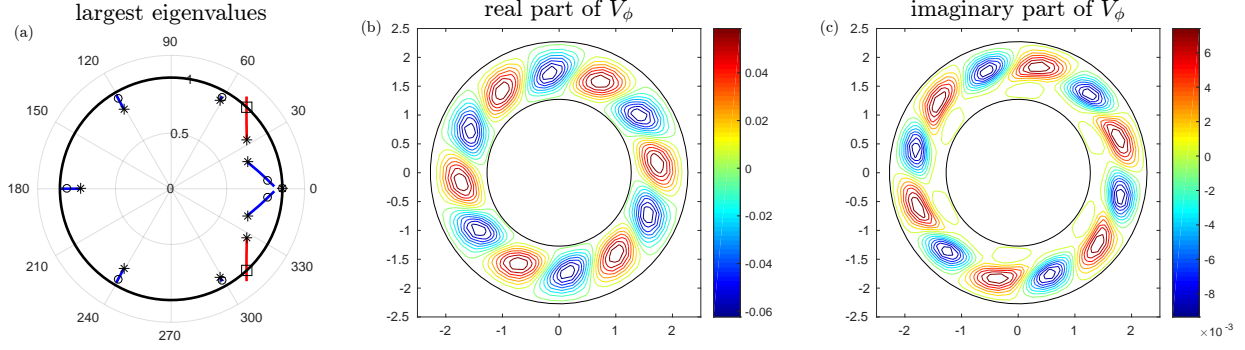


FIG. 4. (a) The evolution of the eigenvalues of the linearization of the map Φ_{τ_w} along the solution branch of the rotating waves. The 10 largest eigenvalues with respect to modulus are depicted for Rayleigh number $602 \leq \mathcal{R} \leq 650$. At $\mathcal{R}_{c2} = 636.2$, the critical eigenvalues are marked with a square, while the others eigenvalues are marked with a circle; all eigenvalues are marked with a star at $\mathcal{R} = 602$. The real and imaginary parts of V_ϕ , the ϕ component of the eigenfunction corresponding to the critical eigenvalues at $\mathcal{R} = \mathcal{R}_{c2}$, are plotted in (b) and (c), respectively.

The arbitrary time for the continuation of the rotating waves (i.e. of the flow map Φ_t) is taken to be $t = 0.1$ with time step $\delta t = 10^{-4}$, while the time step for the computation of the preconditioner is $\delta t_P = 10^{-3}$. The parameters t and δt_P are chosen to maximize efficiency, while still enabling convergence. In particular, choosing a $\delta t_P > 10^{-3}$ does not produce an effective preconditioner, while choosing it smaller does not significantly improve the effectiveness of the preconditioner. The preconditioner computed at $\mathcal{R} = 600$ is used for the entire rotating wave solution branch. The results are not sensitive to the choice of t . Each point on the solution branch $\{(\mathbf{u}_j, w_j, \mathcal{R}_j)\}$ is obtained by using the Newton-Raphson solver to correct an initial guess to within the desired residual tolerance of 10^{-8} in the infinity norm. The initial guess is obtained by following a secant to the branch which is computed from the two previous (known) points on the branch. The initial guess for the first two points on the branch is obtained by time stepping a random initial condition for $t = 10$, with $\mathcal{R} = 600$. At this parameter value the solution associated with the flow of rotating waves is stable and the time integration produces a sufficiently good guess to obtain convergence of the Newton-Raphson iterations. Along the solution branch, convergence in approximately three Newton-Raphson iterations is obtained when the parameter is incremented by $\delta \mathcal{R} = 1$. Each point on the branch is tested for accuracy by integration over the full period τ_w of the solution; each point on the branch is a fixed point of the map Φ_{τ_w} to an error of less than

10^{-4} in the infinity norm. A secant method to a tolerance of 10^{-2} in the parameter \mathcal{R} is used to locate the bifurcation point $\mathcal{R} = \mathcal{R}_{c2}$.

C. Amplitude-modulated waves and the tertiary transition

We continue the amplitude-modulated waves in $\mathcal{R} > \mathcal{R}_{c2}$ by solving (29) using Newton-Raphson iteration with natural continuation, i.e. with \mathcal{R} fixed at each point along the solution branch. Initial guesses of the first two points on the solution branch are found from time-integration of a random initial guess at $\mathcal{R} = 648$. As in the case for the rotating waves, for this value of the parameter, time-integration leads to sufficient decay of transients because the solution is stable. Initial guesses for all other points along the curve are found by following a secant to the solution branch which is computed from the previous two points along the curve. Relative to the rotating wave case, smaller increments $\delta\mathcal{R} = 1/4$ of the parameter along the solution curve are required to obtain adequate initial guesses for the Newton-Raphson iteration to converge. In addition, it is necessary to recompute preconditioning matrices every several steps along the solution branch with a reduced time-step of $\delta t_P = 5 \times 10^{-4}$. These factors, along with the requirement that the integration time be that of the period τ of the amplitude oscillations, lead to a significantly more intensive computational task, relative to the computation of the rotating waves.

Once the solution of (29) is found for a given value of the parameter \mathcal{R} , the equations are integrated over the period τ and a maximum and minimum of the wave amplitude are computed. These values are plotted in the bifurcation diagram of Figure 2. It can be seen that the range of the wave amplitude grows quickly as \mathcal{R} is incremented from $\mathcal{R}_{c2} = 636.2$, then as the minimum amplitude approaches zero, begins to grow more slowly. Figure 5 shows the variation of the amplitude (spatial maximum of the absolute value of the stream function deviation $\phi^{(1)}$) as a function of time over a single period of the amplitude, as well as the period of the amplitude oscillations as \mathcal{R} is varied. The phase speed w (not shown) decreases monotonically from 5.43 at $\mathcal{R} = 644$ to 5.08 at $\mathcal{R} = 682$, where, initially, the slope is relatively flat but becomes steeper as \mathcal{R} is increased. For values of the parameter $\mathcal{R} < 644$, errors are introduced to the calculation of the phase speed and period of amplitude oscillation due to the small variation of amplitude.

The stability of the amplitude-modulated waves is found from the spectrum of $\gamma^{-1}D_{\mathbf{u}}\Phi_{\tau}$,

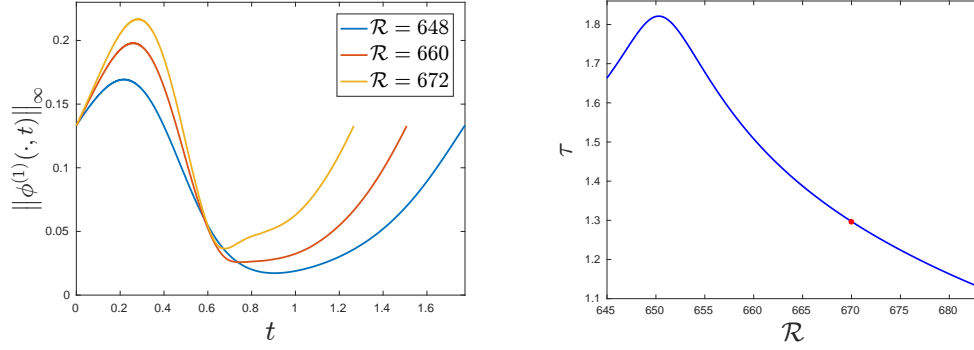


FIG. 5. Amplitude-modulated rotating wave. Left panel: $\|\phi^{(1)}(\cdot, t)\|_\infty$, the infinity norm of the stream function deviation at a particular time (spatial maximum of $|\phi^{(1)}|$), i.e. the wave amplitude, as a function of time t over one period of the amplitude oscillations; results at three different values of the Rayleigh number \mathcal{R} are plotted. Right panel: The period τ of the amplitude oscillations as a function of \mathcal{R} ; the red dot indicates the period at $\mathcal{R} = \mathcal{R}_{c3} = 669.9$.

where τ is the period of the amplitude oscillations and γ is the rotation operator through angle $\theta = w\tau$ (see Section IV D). The 10 eigenvalues with largest magnitude are computed at each point along the branch; their dependence on \mathcal{R} is plotted in Figure 6. Application of the secant method finds a tertiary transition at $\mathcal{R}_{c3} = 669.9$; see Figure 2. In particular, a Neimark-Sacker bifurcation of the map $\gamma^{-1}\Phi_\tau$ occurs as a complex conjugate pair of eigenvalues crosses the $|z| = 1$ curve in the complex plane, while all other eigenvalues have magnitude less than or equal to 1 [42]. As such, we might expect a three-frequency flow to exist close to the bifurcation, although this flow may be dynamically, or structurally, unstable. However, further inspection of Figure 6 reveals that the critical eigenvalues $\lambda_{1,2} = 0.12 \pm i0.99$ are very close to purely imaginary, and thus the bifurcation is very close to having a strong 1:4 resonance. There is a rich variety of behaviour that may be seen near such a bifurcation, including period-4 cycles and heteroclinic connections [40]. However, uncovering the details would require the prohibitively enormous task of computing normal form coefficients. Furthermore, there is also an eigenvalue $\lambda_3 = -0.95$, which is very close to the -1 required for a flip (or period-doubling) bifurcation. Because we can only obtain a rough estimate of the precision of our eigenvalues and we are close to higher co-dimension bifurcations, we cannot be certain of the exact form of the bifurcating solutions.

Thus, we investigate whether simulations of the initial value problem (i.e. time-stepping alone) can reveal any additional information that can verify the nature of the bifurcation.

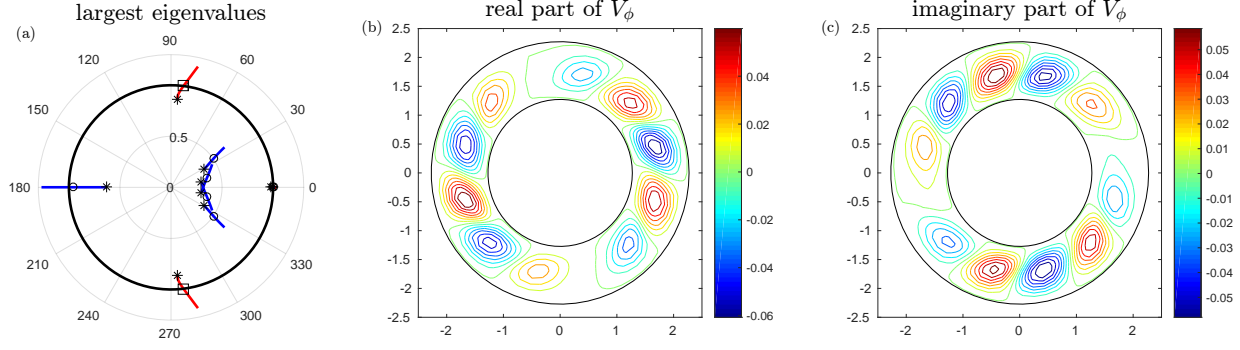


FIG. 6. (a) The evolution of the eigenvalues of $\gamma^{-1} D_{\mathbf{u}} \Phi_{\tau}$ along the solution branch of the amplitude-modulated rotating waves. The 9 largest eigenvalues with respect to modulus are depicted for Rayleigh number $661 \leq \mathcal{R} \leq 681$. At $\mathcal{R}_{c3} = 669.9$, the critical eigenvalues are marked with a square, while the others eigenvalues are marked with a circle; all eigenvalues are marked with a star at $\mathcal{R} = 661$. The real and imaginary parts of V_{ϕ} , the ϕ component of the eigenfunction corresponding to the critical eigenvalues at $\mathcal{R} = \mathcal{R}_{c3}$, are plotted in (b) and (c), respectively.

The initial condition for the simulations is taken to be the end point of the simulation at the previously computed Rayleigh number, and we visualize solutions only for $t > 100$ to ensure that transients have been dampened. The results that are presented in Figures 7 and 8 show the electric Nusselt number as a function of time computed from solutions at Rayleigh numbers close to the critical Rayleigh number $\mathcal{R}_{c3} = 669.9$. The electric Nusselt number is a nondimensional parameter that is defined as the ratio of the total current to the ohmic conduction current, and can be computed from

$$Nu = \frac{\int_0^{2\pi} (u_r q - \partial_r \psi_2) r d\theta}{\int_0^{2\pi} (-\partial_r \psi_2^{(0)}) r d\theta}. \quad (30)$$

Experimental results are often presented in terms of the Nusselt number as it can be calculated directly from current measurements. For more detail see [17]. Because the Nusselt number is computed as an integration over all the domain, the azimuthal variation of the rotating wave is averaged out. Thus, the quasiperiodic nature of the amplitude-modulated wave is hidden, and therefore, it is a good measure for detecting bifurcations from the amplitude-modulated wave. Observations of the time variation of the Nusselt number can provide similar information as those of the norm of the solution, or those of the spatial maximum of one of the components of the solution, e.g. the stream function ϕ .

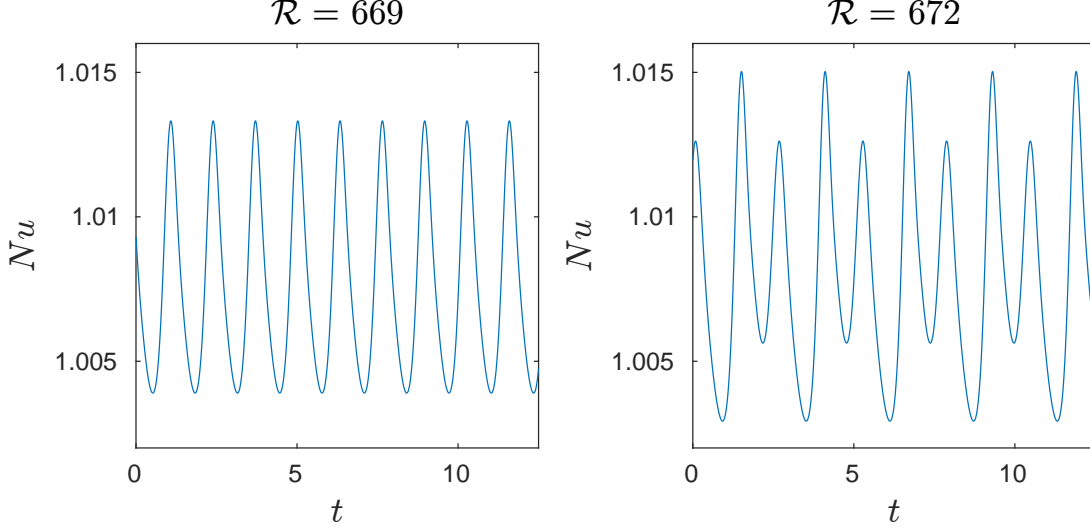


FIG. 7. The Nusselt number Nu as a function of time close to the tertiary transition. Left panel: (before transition) amplitude-modulated rotating wave at $\mathcal{R} = 669$; Right panel: (after transition) amplitude-modulated rotating wave at $\mathcal{R} = 672$, with period four times longer than before transition.

The simulations reproduce the amplitude-modulated rotating wave for $\mathcal{R} = 669 < \mathcal{R}_{c3}$, while the solution for $\mathcal{R} = 672 > \mathcal{R}_{c3}$ is a stable flow that resembles an amplitude-modulated rotating wave with an amplitude that oscillates twice before returning to its initial amplitude (see Figure 7); this pattern is repeated throughout the duration of the simulation (i.e. over 40 cycles). This flow also exhibits a more pronounced tilting of the vortices at the lowest amplitudes. See Supplemental Material at [URL will be inserted by publisher] for an animation of the stream function deviation $\phi^{(1)}$ corresponding to the solution at $\mathcal{R} = 672$. This flow is observed throughout the interval $670 < \mathcal{R} < 674$, and, as the parameter is increased, transitions smoothly from the flow observed before the transition, providing evidence that the bifurcation is supercritical. At first glance, Figure 7 seems to indicate that a flip (or period-doubling) bifurcation rather than the predicted Neimark-Sacker bifurcation occurs at \mathcal{R}_{c3} . However, because the Nusselt number is computed as an integral over the annulus, it does not reveal that for these solutions $\Phi_{2\tau}(\mathbf{u}) \neq \gamma_{2w\tau}\mathbf{u}$, where γ_θ is rotation by θ , i.e. these solutions are not modulated waves with period of amplitude oscillations twice that of the modulated waves observed before transition, see (29). Rather, we have that $\Phi_{2\tau}(\mathbf{u}) = -\gamma_{2w\tau}\mathbf{u}$ or $\Phi_{2\tau}(\mathbf{u}) = \gamma_{\pi/2}\gamma_{2w\tau}\mathbf{u}$, and thus, $\Phi_{4\tau}(\mathbf{u}) = \gamma_{4w\tau}\mathbf{u}$, are approximately

satisfied. That is, the flow is not close to a period-2 cycle of $\gamma^{-1}\Phi_\tau$, but rather a period-4 cycle, as might occur close to bifurcations with 1:4 resonance [40].

The simulations for $\mathcal{R} = 669$ and $\mathcal{R} = 672$ have been verified by repeating the computations using grid size reduced by a factor of two (i.e. using $N_c = 48$ and $K = 64$, see table I, resulting in an increase in the number of grid points by a factor of four). The results found using the finer grid are qualitatively the same, which provides evidence that a transition of the same type occurs for $669 < \mathcal{R} < 672$. Furthermore, the results shown in Figure 7 are also quantitatively comparable to less than 2%, specifically, for the period of oscillation and maximum value of the Nusselt number Nu . The linear stability analysis was not computed on the finer grid, because the computation of the preconditioning matrix was prohibitively long.

These observations are consistent with the linear stability computations discussed above. The critical eigenfunction, associated with the critical eigenvalue $\lambda_1 = 0.12 + i0.99$, looks like a wave with wave number 5, but with two pairs of cells elongated relative to the other cell; see Figure 6. The cells that are not elongated appear to have the same size as those with azimuthal wave number 6, while the elongated cells are approximately twice as large. Thus, it resembles a wave with wave number 6 additively coupled to one with wave number 1. The imaginary part of the eigenfunction resembles the real part, but rotated by an angle of $\pi/2$. The value of the critical eigenvalue λ_1 , in particular that it is close to $e^{i\pi/2}$, and the form and symmetry of the critical eigenfunction indicate how the amplitude (and Nusselt number) oscillations appear to undergo a period doubling. In particular, the interference of the bifurcating instability (i.e. the perturbation from the amplitude-modulated wave) with the amplitude-modulated wave will still resemble a wave number 6 wave. After one period (i.e. one iteration of the map $\gamma^{-1}\Phi_\tau$), the pattern will be different than after 2 periods, when, to first order, it will resemble the initial flow, but rotated by an angle of $\pi/2$ (or multiplied by -1). That is, the amplitude (and Nusselt number) will return to its initial value after two periods, even though the solution itself does not. Two additional periods return the flow, at least approximately, to its initial form.

For $\mathcal{R} > 674$, the flow no longer appears to correspond to a period-4 cycle of $\gamma^{-1}\Phi_\tau$. In particular, an apparent three-frequency flow is observed, in which lower frequency oscillations in the peak amplitude can be seen (see Figure 8). See also Supplemental Material at [URL will be inserted by publisher] for an animation of the stream function deviation $\phi^{(1)}$ for

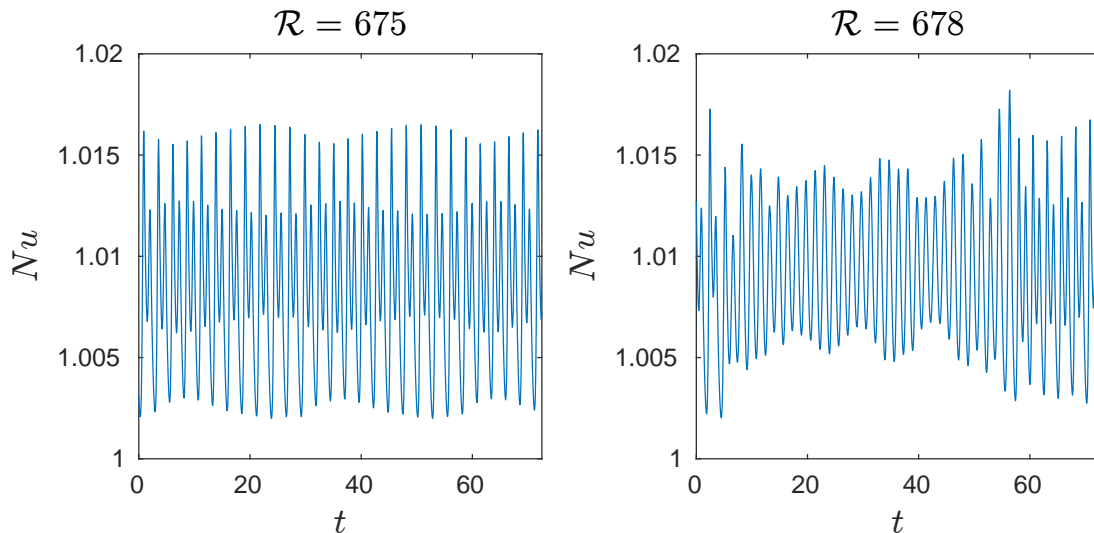


FIG. 8. The Nusselt number Nu as a function of time after the tertiary transition. Left panel: at Rayleigh number $\mathcal{R} = 675$ (modulated amplitude vacillation); Right panel: at Rayleigh number $\mathcal{R} = 678$ (apparently irregular flow). See Supplemental Material at [URL will be inserted by publisher] for animations of the stream function deviation $\phi^{(1)}$ for the corresponding solutions.

the solution at $\mathcal{R} = 675$. It is not clear whether these oscillations are present, but not observable, at smaller values of \mathcal{R} , or whether this is the result of another bifurcation, e.g. a Neimark-Sacker bifurcation from the solution corresponding to the period-4 cycle observed for $670 < \mathcal{R} < 674$. This type of flow has been called modulated amplitude vacillation and has been observed in both experiment and simulation of the differentially heated rotating fluid annulus; see, e.g., [43–46].

The modulated amplitude vacillation solution is observed for only a small interval of the Rayleigh number. A small increase to $\mathcal{R} = 678$ leads to what appears to be a transition to irregular flow. The flow itself begins to show characteristics of mode interaction (e.g. with a wave of wave number 5). However, the simulations did not reveal the nature of this transition. See Supplemental Material at [URL will be inserted by publisher] for an animation of the stream function deviation $\phi^{(1)}$ for the solution at $\mathcal{R} = 678$.

The results presented in Figure 8 resemble those observed in [46], where numerical simulations of the differentially heated rotating annulus reveal a bifurcation sequence similar to that observed in the logistic map. Our results may provide some insight into the origin of this behaviour, which warrants further investigation.

VI. CONCLUSION

In this study, we use numerical bifurcation techniques to study the flow transitions that occur in a mathematical model of sheared annular electroconvection as the electric Rayleigh number \mathcal{R} is increased. A pseudo-spectral time-stepping code, that models the motion of the thin film, is used to approximate a flow map $\Phi_t(\mathbf{u})$ that gives the solution of the model equations at time t for initial conditions \mathbf{u} . The axisymmetric flow, rotating waves, and amplitude-modulated waves observed in the physical system, which, in the model equations, correspond to steady solutions, limit cycles and invariant 2-tori, respectively, are computed as fixed points of this flow map. The approach exploits the fact that the rotating waves are relative equilibria, which enables the extension of such methods to the continuation of the amplitude-modulated rotating waves.

The Newton-Krylov numerical continuation and linear stability analysis that are implemented require only knowledge of the map $\Phi_t(\mathbf{u})$, and does not require access to a linearized code. That is, we consider $\Phi_t(\mathbf{u})$ as a black box, and all computations of the solutions and eigenvalues are accomplished solely by evaluations of Φ_t . This distinguishes this study from [26], the previous study that uses a similar approach to perform numerical continuation of amplitude-modulated rotating waves. This aspect may enable a more straightforward implementation on other problems.

Unlike in previous similar applications of these methods, we do not obtain reasonable convergence of the GMRES iterations [19, 26], during the solution of the linear systems for the Newton-Raphson iterates, without the use of a preconditioner. This may be due to the nonlocal nature of the coupling of the charge density through the 3D electric potential. Our preconditioner is naively computed as a direct approximation of the matrix involved in the linear equations, but is used for all Newton-Raphson iterations across a range of parameter values. Although this preconditioner is very effective across a range of parameters, its computation is a major contribution to the overall time of computation, and therefore it would be useful to have a better means of computing a preconditioning matrix.

The numerical methods locate a sequence of three flow transitions as the Rayleigh number \mathcal{R} is increased. The primary transition, which is a transition from axisymmetric to rotating wave flow, is shown to occur at the critical Rayleigh number, $\mathcal{R}_{c1} = 573.0$, with a critical azimuthal wave number, $m_c = 6$, for the parameters in Table I. These results are in

agreement with those obtained experimentally [11, 12], analytically [10, 30], and using direct numerical simulation [14, 15, 17]. The secondary transition to the amplitude-modulated waves is identified at $\mathcal{R}_{c_2} = 636.2$, and the tertiary transition occurs as the amplitude-modulated waves lose stability at $\mathcal{R}_{c_3} = 669.9$. We have confirmed these results by both qualitative and quantitative comparison to direct numerical simulation computed with a numerical grid size reduced by a factor of two. The computed values for the secondary and tertiary transitions cannot be quantitatively compared to previous studies that have used direct numerical simulation [14, 17] due to the difference in some parameters of the system. The different choice of parameters may also lead to the observed differences in the qualitative features of the tertiary transition. In particular, we observe a period-4-type bifurcation from the amplitude-modulated waves, which has not previously been reported. This observation follows from the prediction, due to the linear stability analysis, that the tertiary transition occurs close to a 1:4 strongly resonant Neimark-Sacker bifurcation of the corresponding flow map.

The flows observed near the tertiary transition greatly resemble flows of interest that have been observed in various differentially heated rotating systems. In particular, we observe flows that resemble the modulated amplitude vacillation seen in [43–46], and those that result from the sequence of bifurcations observed in [46]. This presents an opportunity to study such flows, and the progression to more complex flows in general, in a two-dimensional system.

We have shown the feasibility and validity of the application of numerical bifurcation techniques to sheared annular electroconvection. This motivates an extensive bifurcation analysis of the system that includes the exploration of the effects of other nondimensional parameters (e.g. the Reynolds number Re , the aspect ratio α , and the Prandtl number \mathcal{P}), and the study of other interesting flows that have previously been observed. Of particular interest are rotating waves consisting of isolated or elongated vortices [14, 17], because their origin and nature are not understood. Such studies will help develop an understanding of this complex and interesting system. Due to its analogy with the differentially heated rotating annulus, the results may also provide insight into the nature of flows and transitions observed in differentially heated rotating fluids in general.

ACKNOWLEDGMENTS

M.P. thanks Peichun Tsai for sharing her code to be developed and extended. M.P. thanks Genevieve Bourgeois for her summer Master's project testing the code's convergence and performance in various regimes. G.M.L. would like to acknowledge support from the Natural Sciences and Engineering Research Council of Canada (NSERC), [funding reference number 006257].

- [1] R. Hide and P. Mason, Sloping convection in a rotating fluid, *Adv. Geophys.* **24**, 47 (1975).
- [2] P. Hignett, A. A. White, R. D. Carter, W. D. N. Jackson, and R. M. Small, A comparison of laboratory measurements and numerical simulations of baroclinic wave flows in a rotating cylindrical annulus, *Quart. J. Roy. Meteorolog. Soc.* **111**, 131 (1985).
- [3] P. Read, Transition to geostrophic turbulence in the laboratory, and as a paradigm in atmospheres and oceans, *Surv. Geophys.* **22**, 265 (2001).
- [4] G. M. Lewis and W. Nagata, Double hopf bifurcations in the differentially heated rotating annulus, *SIAM Journal on Applied Mathematics* **63**, 1029 (2003).
- [5] G. M. Lewis, Mixed-mode solutions in an air-filled differentially heated rotating annulus, *Physica D* **239**, 1843 (2010).
- [6] D. Fultz, Developments in controlled experiments on larger scale geophysical problems (Elsevier, 1961) pp. 1–103.
- [7] A. Alonso, M. Net, and E. Knobloch, On the transition to columnar convection, *Physics of Fluids* **7**, 935 (1995), <https://doi.org/10.1063/1.868569>.
- [8] A. Alonso, M. Net, I. Mercader, and E. Knobloch, Onset of convection in a rotating annulus with radial gravity and heating, *Fluid Dynamics Research* **24**, 133 (1999).
- [9] M. Cross and H. Greenside, *Pattern Formation and Dynamics in Nonequilibrium Systems* (Cambridge University Press, 2009).
- [10] Z. A. Daya, V. B. Deyirmenjian, and S. W. Morris, Electrically driven convection in a thin annular film undergoing circular Couette flow, *Physics of Fluids* **11**, 3613 (1999).
- [11] Z. A. Daya, V. B. Deyirmenjian, and S. W. Morris, Bifurcations in annular electroconvection with an imposed shear, *Physical Review E* **64**, 036212 (2001).

- [12] Z. A. Daya, V. B. Deyirmenjian, S. W. Morris, and J. R. De Bruyn, Annular electroconvection with shear, *Physical Review Letters* **80**, 964 (1998).
- [13] V. B. Deyirmenjian, Z. A. Daya, and S. W. Morris, Codimension-two points in annular electroconvection as a function of aspect ratio, *Physical Review E* **72**, 036211 (2005).
- [14] P. Tsai, Z. A. Daya, V. B. Deyirmenjian, and S. W. Morris, Direct numerical simulation of supercritical annular electroconvection, *Physical Review E* **76**, 026305 (2007).
- [15] P. Tsai, S. W. Morris, and Z. A. Daya, Localized states in sheared electroconvection, *EPL (Europhysics Letters)* **84**, 14003 (2008).
- [16] P. Tsai, Z. A. Daya, and S. W. Morris, Aspect-ratio dependence of charge transport in turbulent electroconvection, *Physical Review Letters* **92**, 084503 (2004).
- [17] P.-C. Tsai, *The Route to Chaos and Turbulence in Annular Electroconvection*, Ph.D. thesis, University of Toronto (2007).
- [18] H. Dijkstra, F. Wubs, A. Cliffe, E. Doedel, I. Dragomirescu, B. Eckhardt, A. Gelfgat, A. Hazel, V. Lucarini, A. Salinger, E. Phipps, J. Sanchez, H. Schuttelaars, L. Tuckerman, and U. Thiele, Numerical bifurcation methods and their application to fluid dynamics: Analysis beyond simulation, *Communications in Computational Physics* **15**, 1 (2014).
- [19] J. Sánchez, M. Net, B. Garcia-Archilla, and C. Simó, Newton–Krylov continuation of periodic orbits for Navier–Stokes flows, *Journal of Computational Physics* **201**, 13 (2004).
- [20] J. Sánchez, M. Net, and C. Simó, Continuation of invariant tori by Newton-Krylov methods in large-scale dissipative systems, *Physica D* **239**, 123 (2010).
- [21] L. S. Tuckerman and D. Barkley, Bifurcation analysis for timesteppers, in *Numerical Methods for Bifurcation Problems and Large-Scale Dynamical Systems*, IMA Volumes in Mathematics and its Applications, Vol. 119, edited by E. Doedel and L. Tuckerman (Springer–Verlag, 2000) Chap. 8, p. 453–466.
- [22] I. Mercader, O. Batiste, and A. Alonso, Continuation of travelling-wave solutions of the Navier-Stokes equations, *International Journal for Numerical Methods in Fluids* **52**, 707 (2006).
- [23] D. Viswanath, Recurrent motions within plane Couette turbulence, *Journal of Fluid Mechanics* **580**, 339 (2007).
- [24] J. Sánchez, F. Garcia, and M. Net, Computation of azimuthal waves and their stability in thermal convection in rotating spherical shells with application to the study of double-Hopf bifurcation, *Physical Review E* **87**, 1 (2013).

- [25] G. Kawahara, M. Uhlmann, and L. van Veen, The significance of simple invariant solutions in turbulent flows, *Annual Review of Fluid Mechanics* **44**, 203 (2012).
- [26] F. Garcia, M. Net, and J. Sánchez, Continuation and stability of convective modulated rotating waves in spherical shells, *Physical Review E* **93**, 1 (2016).
- [27] D. A. Saville, Electrodynamics: The Taylor-Melcher leaky dielectric model, *Annual Review of Fluid Mechanics* **29**, 27 (1997), <https://doi.org/10.1146/annurev.fluid.29.1.27>.
- [28] S. W. Morris, J. R. de Bruyn, and A. D. May, Patterns at the onset of electroconvection in freely suspended smectic films, *Journal of Statistical Physics* **64**, 1025 (1991).
- [29] S. S. Mao, J. R. de Bruyn, and S. W. Morris, Boundary-induced wavelength selection in a one-dimensional pattern-forming system, *arXiv preprint patt-sol/9503002* (1995).
- [30] Z. A. Daya, S. W. Morris, and J. R. de Bruyn, Electroconvection in a suspended fluid film: a linear stability analysis, *Physical Review E* **55**, 2682 (1997).
- [31] V. B. Deyirmenjian, Z. A. Daya, and S. W. Morris, Weakly nonlinear analysis of electroconvection in a suspended fluid film, *Physical Review E* **56**, 1706 (1997).
- [32] Z. A. Daya, V. B. Deyirmenjian, and S. W. Morris, Sequential bifurcations in sheared annular electroconvection, *Physical Review E* **66**, 015201 (2002).
- [33] R. Peyret, *Spectral Methods for Incompressible Viscous Flows*, Vol. 148 (Springer, New York, 2002).
- [34] J. Varah, Stability restrictions on second order, three level finite difference schemes for parabolic equations, *SIAM Journal on Numerical Analysis* **17**, 300 (1980).
- [35] U. Ascher, S. Ruuth, and B. Wetton, Implicit-explicit methods for time-dependent partial differential equations, *SIAM Journal on Numerical Analysis* **32**, 797 (1995).
- [36] In [17], the stream function was split into base state and deviation parts, $\phi = \phi^{(0)} + \phi^{(1)}$. Then $\phi^{(0)}$ was treated exactly, while the boundary conditions on the deviation part were assumed to be $\phi^{(1)}(r_i, \theta) = \phi^{(1)}(r_o, \theta) = 0$. The ODE (11) was neither derived nor time-stepped. This is equivalent to setting $g^{(1)}(t) = 0$. We can quantify the accuracy of this approximation by using our results from section V to numerically calculate the fraction $f = \max(g^{(1)}(t)) / \max(g(t))$ for the various states observed. Referring to figure 2, we find that at $\mathcal{R} = 600$, in the rotating wave regime, $f \approx 3 \times 10^{-5}$, while at $\mathcal{R} = 660$, in the amplitude modulated regime, $f \approx 10^{-4}$. Thus, the simplifying approximation used in [17] is reasonably good, so that no qualitative differences are to be expected between our calculations and theirs. This approximation amounts to adding

an additional physical constraint that the part of the total azimuthal flux not imposed by the rotation of the inner electrode must be zero. As the electrical forces are mainly radial, they evidently do not produce much additional azimuthal flux.

- [37] Y. Saad and M. H. Schultz, GMRES: A generalized minimal residual algorithm for solving nonsymmetric linear systems, *SIAM Journal on Scientific and Statistical Computing* **7**, 856 (1986).
- [38] L. N. Trefethen and D. Bau III, *Numerical Linear Algebra*, Vol. 50 (SIAM, Philadelphia, 1997).
- [39] R. B. Lehoucq, D. C. Sorensen, and C. Yang, *ARPACK Users' Guide: Solution of Large-Scale Eigenvalue Problems with Implicitly Restarted Arnoldi Methods* (SIAM, Philadelphia, 1998).
- [40] Y. A. Kuznetsov, *Elements of Applied Bifurcation Theory*, 2nd ed., Vol. 112 (Springer Science & Business Media, 1998).
- [41] Because $\gamma \mathbf{u}$ is a nontrivial fixed point of the map Φ_{τ_w} , the spectrum of $D_{\mathbf{u}}\Phi_{\tau_w}$ always contains at least one (real) eigenvalue equal to 1.
- [42] Because \mathbf{u} is a fixed point of the map $\gamma^{-1}\Phi_{\tau_w}$, the spectrum of $D_{\mathbf{u}}\Phi_{\tau}$ always contains at least two eigenvalues equal 1, one associated with the phase of the wave and one with the phase of the amplitude oscillation.
- [43] W.-G. Fröh and P. Read, Wave interactions and the transition to chaos of baroclinic waves in a thermally driven rotating annulus, *Philosophical Transactions of the Royal Society of London, A* **355**, 101 (1997).
- [44] A. Randriamampianina, W.-G. Fröh, P. Read, and P. Maubert, Direct numerical simulations of bifurcations in an air-filled rotating baroclinic annulus, *J. Fluid Mech.* **561**, 359 (2006).
- [45] A. Castrejon-Pita and P. Read, Baroclinic waves in an air-filled thermally driven rotating annulus, *Physical Review E* **75**, pp. 10 (2007).
- [46] R. Young and P. Read, Flow transitions resembling bifurcations of the logistic map in simulations of the baroclinic rotating annulus, *Physica D* **237**, 2251 (2008).